# Tractographic and microstructural analysis of the dentato-rubro-thalamo-cortical tracts in healthy children using diffusion MRI

*Sebastian M Toescu[1,2], Patrick W Hales[1], Enrico Kaden[1,3], Luis M Lacerda[1], Kristian Aquilina[2], Christopher A Clark[1]*

1. Developmental Imaging and Biophysics Section, UCL-GOS Institute of Child Health, 30 Guilford St, London, UK, WC1N 1EH
2. Department of Neurosurgery, Great Ormond Street Hospital, London, UK, WC1N 3JH
3. Centre for Medical Image Computing, University College London, London,UK, WC1V 6LJ

Corresponding author:
Sebastian M Toescu, Developmental Imaging and Biophysics Section, UCL-GOS Institute of Child Health, 30 Guilford St, London WC1N 1EH. 0207 242 9789. sebastian.toescu@ucl.ac.uk

## Abstract

The dentato-rubro-thalamo-cortical tract (DRTC) is the main outflow pathway of the cerebellum, contributing to a finely balanced corticocerebellar loop involved in cognitive and sensorimotor functions. Damage to the DRTC has been implicated in cerebellar mutism syndrome seen in up to 25% of children after cerebellar tumour resection. Multi-shell diffusion MRI (dMRI) combined with quantitative constrained spherical deconvolution tractography and multi-compartment spherical mean technique modelling were used to explore the frontocerebellar connections and microstructural signature of the DRTC in 30 healthy children. The highest density of DRTC connections were to the precentral (M1) and superior frontal gyri (F1), and from cerebellar lobules I-IV and IX. The first evidence of a topographic organisation of anterograde projections to the frontal cortex at the level of the superior cerebellar peduncle (SCP) is demonstrated, with streamlines terminating in F1 lying dorsomedially in the SCP compared to those terminating in M1. The orientation dispersion entropy of DRTC regions appears to exhibit greater contrast than that shown by fractional anisotropy. Analysis of a separate reproducibility cohort demonstrates good consistency in the dMRI metrics described. These novel anatomical insights into this well-studied pathway may prove to be of clinical relevance in the surgical resection of cerebellar tumours.[199 words]

## Keywords

Tractography, constrained spherical deconvolution, spherical mean technique, dentato-rubro-thalamo-cortical tract, cerebellar mutism syndrome

## Abbreviations

CSD, constrained spherical deconvolution; CMS, cerebellar mutism syndrome; CSF, cerebrospinal fluid; dMRI, diffusion magnetic resonance imaging; DRTC, dentato-rubro-thalamo-cortical; FA, fractional anisotropy; FSL, FMRIB software library; HARDI, high angular resolution diffusion imaging; ICC, intraclass correlation coefficient; M1, primary motor cortex; MD, mean diffusivity; ODE, orientation dispersion entropy; RN, red nucleus; ROI, region of interest; SCP, superior cerebellar peduncle; SD, standard deviation; SMA, supplementary motor area; SMT, spherical mean technique; SUIT, spatially unbiased infratentorial template; TDI, track density image; TE, echo time; TR, relaxation time; TSC, total streamline count; $V_{int}$, intraneurite volume fraction; 5TT, 5 tissue type.

# Introduction

The dentato-rubro-thalamo-cortical tract (DRTC) is the main outflow pathway of the cerebellum, contributing to a finely balanced corticocerebellar loop involved in cognitive and sensorimotor control (Palesi et al. 2017). Its efferent fibres from the dentate nucleus form the superior cerebellar peduncle (SCP), decussate in the midbrain and ascend via the red nucleus and thalamus before projecting to widespread areas of the cerebral cortex (Palesi et al. 2015). Diffusion MRI (dMRI) is uniquely placed as a non-invasive tool with which to explore the anatomy and underlying microstructure of the tract *in vivo*. Tractography studies have depicted the anatomy of the DRTC (Salamon et al. 2007; Kwon et al. 2011; Mollink et al. 2016), and have offered insights into the precise regions of cortical termination of the tract (Palesi et al. 2015, 2016; Ji et al. 2019) in adults. However, these relationships have yet to be characterised in young children. This is particularly important given the implication of the DRTC in the development of cerebellar mutism syndrome (CMS), seen in up to a quarter of children after midline posterior fossa tumour resection. CMS is a transient yet debilitating post-operative syndrome comprising linguistic, affective and emotional deficits, as well as cerebellar motor signs. Alterations in dMRI metrics of the proximal DRTC in children with CMS have been described (Morris et al. 2009; Law et al. 2012; Soelva et al. 2013; Perreault et al. 2014; McEvoy et al. 2016). A detailed depiction of the entire extent of the DRTC in healthy children will support future comparisons across post-operative paediatric cohorts comprising children with and without CMS.

As well as providing estimates of long-range connectivity via tractography, dMRI is also able to probe the microstructure of the brain. The diffusion tensor (Basser et al. 1994) is the canonical model of dMRI signal. More recent developments in MR acquisition schemes include high angular resolution diffusion imaging (HARDI) methods, in which the diffusion signal is sampled along a uniformly distributed set of directions on the surface of a sphere (the radius of which relates to the degree of diffusion weighting, or 'b-value'). Multiple spheres can be sampled in so-called "multi-shell" acquisitions by applying different b-values, in order to sample the diffusion signal over a greater range of diffusion weightings. This permits the application of more complex biophysical models in post-processing, such as constrained spherical deconvolution (CSD) (Tournier et al. 2004) and the spherical mean technique (SMT) (Kaden, Kelm, et al. 2016), complementary modelling techniques which enable estimation of fibre orientation distribution and microstructural tissue features, respectively.

The aim of this study was to investigate in detail the frontal and cerebellar connections of the DRTC tract, as well as its microstructural signature, in healthy children using dMRI. We hypothesised a significant connection to cortical regions consistent with the supplementary motor area (SMA). If these insights from tractography are to be applied successfully to clinical populations, assessment of the reproducibility of the technique is important (Schilling et al. 2019). Therefore, in this study a separate cohort was included to test the reproducibility of the analysis.

# Methods

## Participants

Thirty healthy children recruited to existing ethically-approved departmental studies were included in this analysis (REC #15/LO/0347 and #14/LO/0115). Fifteen were healthy sickle cell trait carriers, and the remainder were healthy children of staff at our Institution. All were born at full term with no significant medical history, in particular no neurological or psychiatric diagnoses; and no radiological abnormalities were detected on MRI scans. These 30 control subjects' ages ranged between 7.3 and 21.8 years (median 10.7, interquartile range 5.85); 16 were female and 5 were left-handed. A further group of 6 healthy young adult subjects were included who had undergone repeat MRI scanning one week apart using the same scanner and pulse sequences. The six reproducibility subjects had a mean age of 25.5 (S.D. 4.31); 5 were male, all were right-handed.

## MRI acquisition

Imaging was performed on a 3T MRI scanner (MAGNETOM Prisma, Siemens Healthcare, Erlangen, Germany) using a 64 or 20 channel head receive coil. Volumetric T1-weighted (T1w) images were acquired using an MPRAGE (Mugler and Brookeman 1990) sequence with isometric 1.0mm voxels, TR=2300ms, TE=2.74ms, acquisition time 5m21s.

The multi-shell diffusion MRI (dMRI) sequence employed a diffusion-weighted spin-echo single shot 2-dimensional echo planar imaging acquisition, with multi-banded radio frequency pulses to accelerate volume coverage along the slice direction (Auerbach et al. 2013). We employed a multi-band factor of 2 over 66 slices of 2mm thickness with 0.2 mm slice gap. Diffusion gradients were applied over two 'shells': b=1000 s/mm$^2$ and b=2200 s/mm$^2$, with 60 non-collinear diffusion directions per shell, in addition to 13 interleaved b = 0 s/mm$^2$ (non-diffusion weighted) images. Other imaging parameters were: TR=3050ms, TE=60ms, field of view=220x220mm$^2$, matrix size=110x110, in-plane voxel resolution=2.0x2.0mm$^2$, GRAPPA factor 2, phase-encoding (PE) partial Fourier=6/8. An additional b0 acquisition was performed, with identical readout to the diffusion-weighted scan, but with the PE direction flipped by 180° (in the anterior-posterior direction), for correction of susceptibility-related artefacts. Acquisition time, 7m50s.

## Image preprocessing

Raw Dicom images were converted to NIFTI format using TractoR (Clayden et al. 2011). Cortical parcellation and subcortical segmentation were performed on volumetric T1w images using Freesurfer (Dale et al. 1999; Fischl et al. 2002). The parcellation outputs at this point were visually checked for each subject and manually edited where required. The volumetric T1w image was linearly co-registered using *NiftyReg* (Modat et al. 2014) to each subject's non-diffusion weighted image (b0).

The T1-derived parcellation map was then carried over into subjects' diffusion space using the affine transformation generated in the previous step.

Raw dMRI image files were processed using MRtrix (Tournier et al. 2012) (version 3) and FSL (Jenkinson et al. 2012) (version 5.0.10). The data were denoised with *dwidenoise* (Veraart et al. 2016), using a brain mask to improve processing speed, and Gibbs ringing artefacts were corrected with *mrdegibbs* (Kellner et al. 2016). The dMRI data and reverse phase-encode b0 images were processed using FSL's *topup* (Andersson et al. 2003; Smith et al. 2004) and eddy (Andersson and Sotiropoulos 2016) tools to correct for susceptibility-induced distortions, eddy-current artefacts and subject motion. The final step of dMRI preprocessing was B1 field inhomogeneity correction with *dwibiascorrect* (Zhang et al. 2001; Smith et al. 2004). The MRtrix *5ttgen* script employing the *fsl* algorithm (Smith et al. 2012) was used to segment subjects' diffusion-aligned T1w image into five tissue types (5TT; white matter, cortical grey matter, subcortical grey matter, CSF, other).

## Voxel-wise modelling

The diffusion tensor was calculated on a voxel-wise basis using MRtrix' *dwi2tensor* script and DTI parameter maps for fractional anisotropy (FA) and mean diffusivity (MD) were then computed. After adjustment of the diffusion signal to reduce the Rician-noise induced bias(Kaden, Kruggel, et al. 2016), a multi-compartment microscopic diffusion model was fitted using SMT (Kaden, Kelm, et al. 2016) to derive estimates of the intra-neurite volume fraction ($V_{int}$). SMT-based fiber orientation distributions were computed, and from this an index of orientation dispersion entropy (ODE) was calculated in each voxel. The ODE measures the distance (Kullback–Leibler divergence) of an orientation distribution with respect to the uniform distribution. This metric is zero when the orientation distribution under consideration is uniform, and infinite when all fibres have exactly the same orientation. Typical values in the brain range between 0 and 1.5.

## DRTC tractography

Fibre orientation distributions (FODs) were modelled using constrained spherical deconvolution (CSD) (Tournier et al. 2004). Response functions were calculated for each tissue type using the co-registered 5TT image generated in the previous step. From this, voxel-wise estimates of FODs were produced for grey and white matter (Jeurissen et al. 2014).

Whole-brain tractography was performed using a probabilistic algorithm employing second-order integration over FODs (Tournier et al. 2010) (*iFOD2* algorithm). Seeding from the whole brain mask, 3 million streamlines were generated, terminating at FOD amplitudes of less than 0.1. These streamlines were then resampled into a track-density image (TDI) with an isotropic voxel size of 250μm, creating a 'super-resolution' streamline map (Calamante et al. 2010, 2011) to improve contrast within white matter structures. SCP and red nucleus (RN) regions of interest (ROIs) were

placed on 30-35 and 10-15 contiguous axial 'super-resolution' TDI slices respectively, as this form of image contrast has previously been shown to be useful in the manual placement of regions of interest for seeded tractography of cerebellar projections (Palesi et al. 2015, 2016, 2017). The ROIs were drawn and confirmed by neurosurgeons (SMT, KA) familiar with brainstem anatomy. SCP and RN ROIs were registered back into diffusion space for further analysis. Further 'exclusion' ROIs were placed on subjects' FA maps at the corpus callosum and crura of the fornix in the mid-sagittal plane; at the inferior and middle cerebellar peduncles; and the above SCP ROIs were dilated to produce enlarged contralateral SCP exclusion masks (Figure 2).

DRTC tractography was performed seeding bidirectionally from the SCP ROI, with a contralateral RN ROI as a waypoint, and the aforementioned exclusion ROIs. Default parameters including iFOD2 were used, with 5 million seeds. This process was repeated for both left and right DRTC tracts. Finally, visitation maps or track-density images (TDIs) were created of both DRTC tracts, and these were thresholded to a lower limit of 5% of the range of total streamline count (TSC). DRTC tracts with less than 1000 streamlines were discarded from the analysis.

The spatial location of the DRTC within the thalamus was assessed by parcellating the thalamus according to its frontal connectivity using an established winner-takes-all method (Behrens et al. 2003). The whole thalamus and non-overlapping masks of the prefrontal, motor, temporal, parietal and occipital cortical ribbons were extracted from diffusion-registered anatomical parcellations. In addition, two hemispheric cortical masks were created by summing the registered lobar cortical masks. Probabilistic tractography using the CSD-derived FODs was run by seeding 500 streamlines per voxel within the thalamus, terminating at the summed hemispheric cortical mask. This global tractogram was divided up by selecting out streamlines which terminated in each of the target regions, and the end points of these streamlines were mapped within the thalamus, assigning a value to each voxel based on its target region of maximal connectivity.DRTC tract dissection according to frontal and cerebellar connectivity

Masks for regions of left and right frontal cortex specified in Figure 1 were extracted from diffusion-registered anatomical parcellations. DRTC tracts were dissected according to their termination in different frontal region masks. The number of streamlines arriving at each frontal region was normalised by dividing by the total number of streamlines in each subjects' DRTC tract, and then by

the volume of each frontal region to which it arrived, to generate the metric reported below: streamline density. Herein, dissected DRTC streamlines terminating in a given cortical region are termed '*bundles*'; the complete set of reconstructed streamlines is referred to as the DRTC '*tract*'.

The Spatially Unbiased Infratentorial Template toolbox (SUIT; version 3.1) and cerebellar lobule atlas (after Schmahmann et al. 2000) were used to probe connections of the DRTC in the cerebellar cortex. Figure 1 shows the cerebellar regions of interest. SUIT was implemented in SPM12 v7771 (Wellcome Centre for Human Neuroimaging, London, UK) running in Matlab 2017b (MathWorks, Inc., Natick, MA, US). The cerebellum and brainstem were isolated and normalized into SUIT space for each subject. The inverse affine transformation from the normalization step was then used to re-slice the SUIT atlas into subject space. The number of streamlines arriving at each cerebellar lobule were normalised by dividing by the total number of streamlines in each subjects' DRTC tract, and then by the volume of each cerebellar lobule to which it arrived.

Additionally, a binary mask was derived from the entire hemispheric frontal cortical ribbons for each subject, and the intersection of the un-thresholded DRTC TDIs and cortical ribbons found. These intersection maps were registered onto a group template created of all subjects' FA map for visualisation.

## Spatial topography of the DRTC in the superior cerebellar peduncle

Individual subjects' DRTC streamlines terminating in each region of frontal cortex were registered into group template space using the inverse of the warps from template creation. Streamlines terminating in each frontal cortex region were concatenated across all subjects, and each summed regional streamline bundle was resampled to the modal number of vertices for all streamlines in that bundle. An average streamline position was then calculated at each streamline vertex in three dimensions to enable visualisation of an average streamline position for each frontal region of termination. Summed and average regional DRTC streamlines were then viewed in sagittal and cross section to ascertain whether fibres travelling to different regions of the frontal cortex were localised in particular zones of the SCP.

## Statistical analysis

All statistical analysis was performed in R(Team 2017) (v3.6.1) and graphics were created using the ggplot2 (Wickham 2009), rstatix (Kassambara 2020) and ggpubr (Kassambara 2019) packages. Continuous data were assessed for normality using the Shapiro-Wilk test, and t test comparisons were used where this was satisfied. Where this assumption was not met, the Kruskal-Wallis test was used to compare medians across brain regions. Pairwise comparisons between streamline counts to different brain regions were performed with the Wilcoxon signed-rank test as these results were invariably positively skewed. Intraclass correlation coefficient was calculated using a one-way random

model on single measures of scan-rescan data with computation of inter-rater consistency (ICC(1,1)) (Gamer et al. 2019); different scanning sessions were considered as raters. Associated *p* values indicate the probability of obtaining the observed ICC values if the null hypothesis (ICC=0) were true. Multiple comparison correction using the method of Benjamini & Hochberg (Benjamini and Hochberg 1995) was employed throughout to account for all the comparisons across different brain regions.

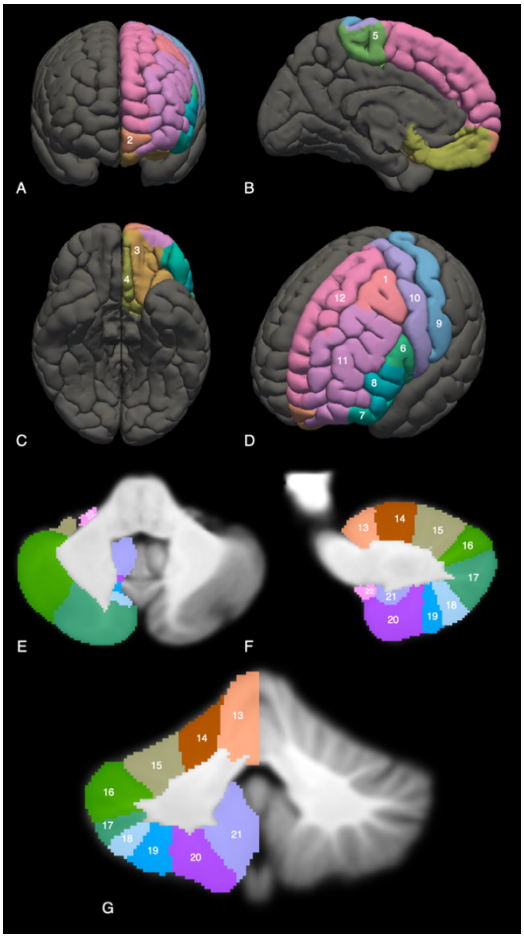


**Figure 1**. Surface representations of a representative subject's frontal cortex regions shown in T1 space in anterior (**A**), medial (**B**), inferior (**C**) and superior oblique (**D**) projections of the left frontal cortex only, for clarity. Volume representations of a representative subject's right cerebellar lobules from the SUIT atlas(Diedrichsen 2006) in axial (**E**), right parasagittal (**F**) and coronal (**G**) projection, overlaid on SUIT-extracted brainstem and cerebellum template in SUIT space. 1, caudal middle frontal gyrus; 2, frontal pole; 3, lateral orbitofrontal cortex; 4, medial orbitofrontal cortex; 5, paracentral lobule; 6, pars opercularis; 7, pars orbitalis; 8, pars triangularis; 9, postcentral gyrus; 10, precentral gyrus; 11, rostral middle frontal gyrus; 12, superior frontal gyrus; 13, lobules I-IV; 14, lobule V; 15, lobule VI; 16, Crus I; 17, Crus II; 18, lobule VIIb; 19, lobule VIIIa; 20, lobule VIIIb; 21, lobule IX; 22, lobule X.

# Results

## DRTC tractography

The DRTC was successfully reconstructed in all subjects bar 2 in whom the right DRTC contained less than 1000 streamlines; these were discarded from analyses. Figure 2 shows relevant ROI placement and resultant DRTC tracts in example subjects. Streamlines ranged from the ipsilateral cerebellar cortex, passed through the SCP and decussated in the pontomesencephalic tegmentum before passing through the contralateral red nucleus and subthalamic region. Streamlines then ascended through the thalamus before spreading out to terminate in widespread regions of contralateral cerebral cortex. The anatomical depiction of DRTC reconstructions was stable across the age ranges seen in the cohort, as evidenced by the similarity of Figure 2B and 2C. Visualisation of the DRTC within the thalamus showed that DRTC streamlines overlapped with regions of the thalamus which had predominant connections to the frontal and motor cortices, and this was also stable across the age spectrum.

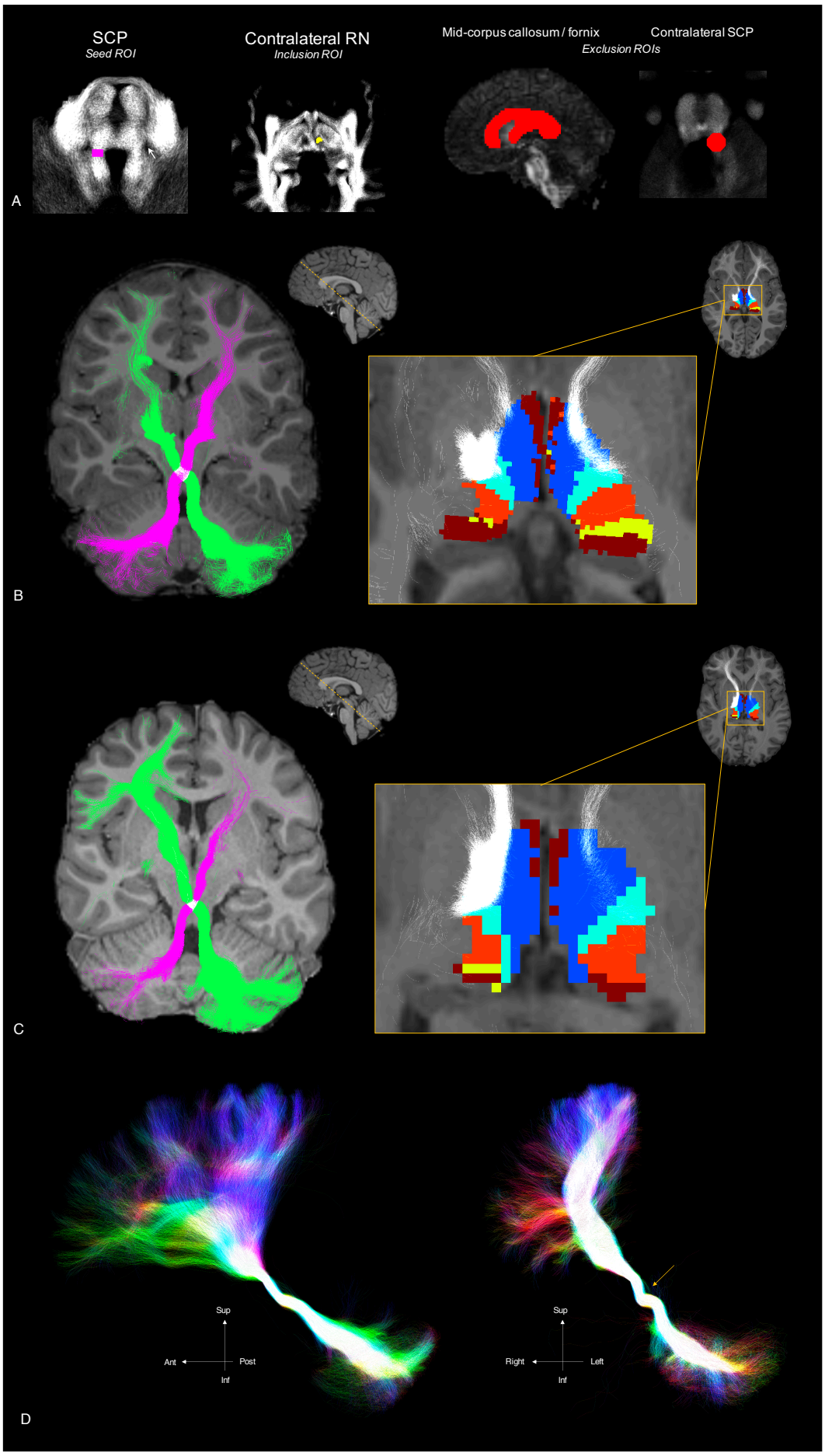
SCP
Seed ROI
Contralateral RN
Inclusion ROI
Mid-corpus callosum / fornix
Contralateral SCP
Exclusion ROIs
A
B
C
D
Sup
Ant
Post
Inf
Sup
Right
Left
Inf

1

**Figure 2**. Example of DRTC ROI placement and tractography results in representative subjects. **A (left)**, seed ROI placed at the superior cerebellar peduncle (SCP) on axial 'super-resolution' track-density image (TDI), on 30-35 contiguous axial slices beginning caudally at the level of the parabrachial recess (white arrow). **A (centre)**, waypoint ROI placed at the contralateral red nucleus (RN) on the axial 'super-resolution' TDI. **A (right)**, exclusion ROIs placed at the mid-corpus callosum and midline fornix (left, sagittal FA map) and on the contralateral SCP (right, axial 'super-resolution' TDI). **B**, tractography results for the youngest subject in the cohort (age 7.2y). **B (left)**, tractography streamlines for left (green) and right (pink) DRTC reconstructions displayed along the long axis of the tract (dashed yellow line in inset). **B (right)**, overlap of DRTC streamlines within thalamus parcellated according to cortical connectivity (blue, frontal; light blue, motor; orange, parietal; yellow, occipital; red, temporal) shown on a mid-thalamic axial slice. **C**, results shown as per B, but for the oldest subject in the cohort (age 21.8y). **D**, Volume rendering of left DRTC tract viewed in sagittal (**D, left**) and coronal (**D, right**) projections, with streamline colour encoding direction (green, anteroposterior; red, lateral; blue, superoinferior). Decussation of the DRTC at the midline can be clearly seen at the yellow arrow.

## Dissection of DRTC tractography

Across the 30 subjects studied, the highest density of DRTC streamline terminations appeared to be in the precentral gyrus, followed by the SMA extending rostrally along the superior frontal gyrus (Figure 3). A quantitative analysis of these connections is shown in Figure 4A and B. Streamline density to the frontal cortex was highest in the precentral gyrus and the superior frontal gyrus for both right and left DRTC tracts. Pairwise comparison testing confirmed that these two regions had significantly higher streamline density than almost all other regions, on both sides; and that the orbitofrontal gyri and pars opercularis had significantly lower streamline density than most other regions (Figure 5A, B).

Both right and left DRTC tracts had a strikingly higher number of streamlines terminating in the anterior cerebellum (lobes I-IV) and in lobule IX than in other cerebellar regions (Figure 4C,D). Formal statistical testing using Wilcoxon pairwise comparisons confirmed this association (Figure 5C, D).

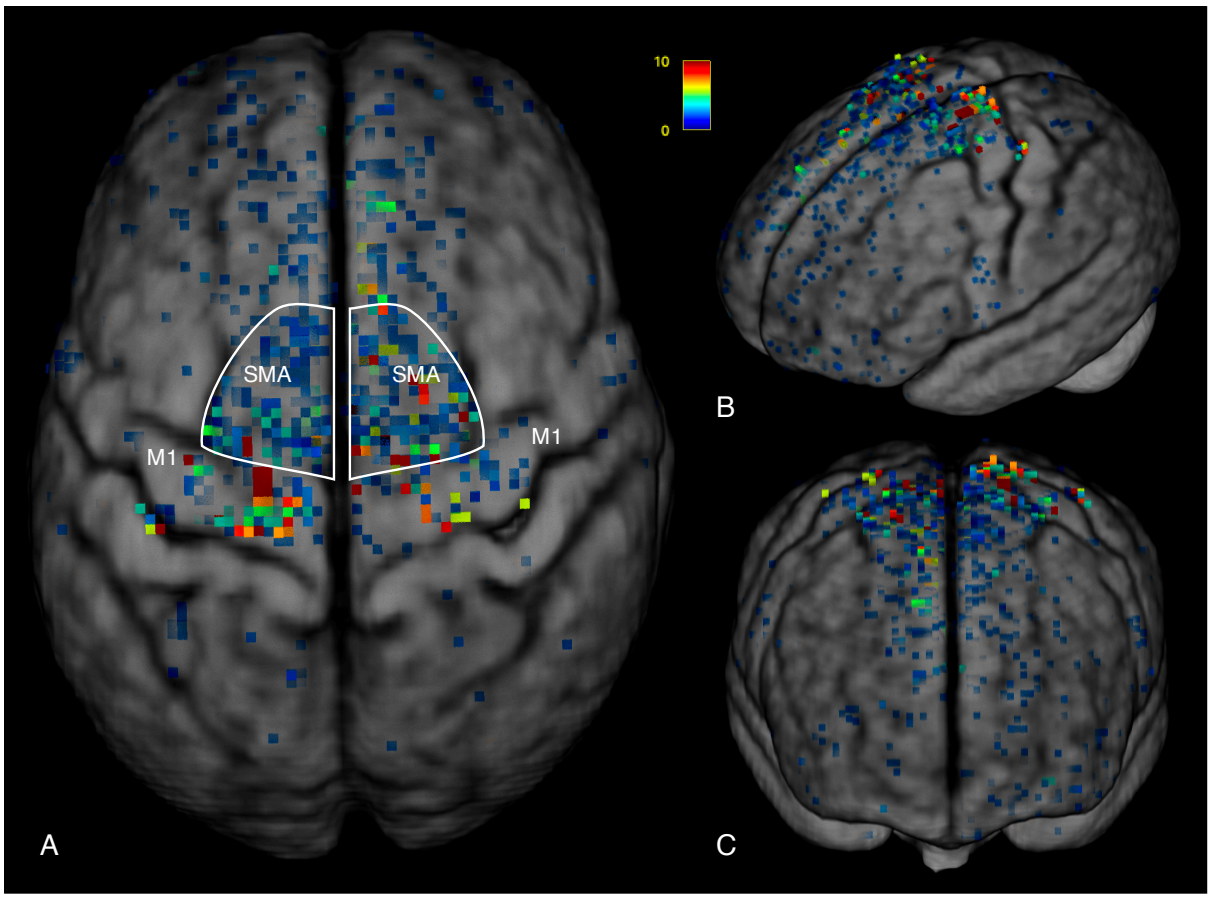


**Figure 3**. Unconstrained cortical terminations of right and left DRTC displayed on a group template in diffusion space. **A**, superior; **B,** frontal; **C**, left supero-lateral projection. The highest density of streamline terminations is in the precentral gyrus (M1) and supplementary motor area (SMA). Scale bar indicates number of streamlines terminating in a given voxel.

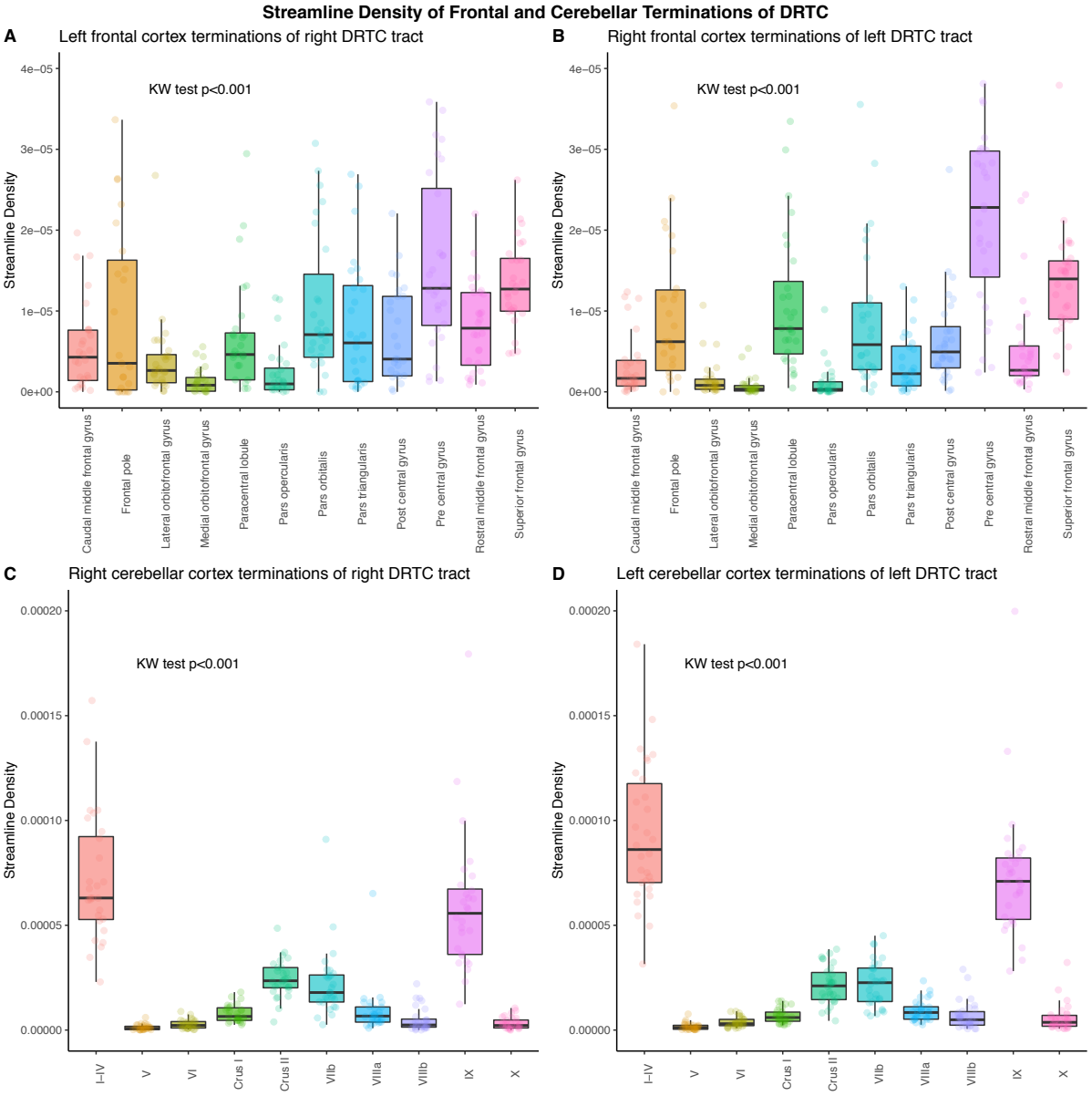


**Figure 4**. Box- and dot-plots of streamline density by region of frontal and cerebellar cortical termination. **A**, left frontal cortex terminations of right DRTC tract. **B**, right frontal cortex terminations of left DRTC tract. **C**, right cerebellar cortex terminations of right DRTC tract. **D**, left cerebellar cortex terminations of left DRTC tract. Boxes show interquartile range, and median streamline densities. Kruskal-Wallis test *p* value < 0.001 for all 4 plots.

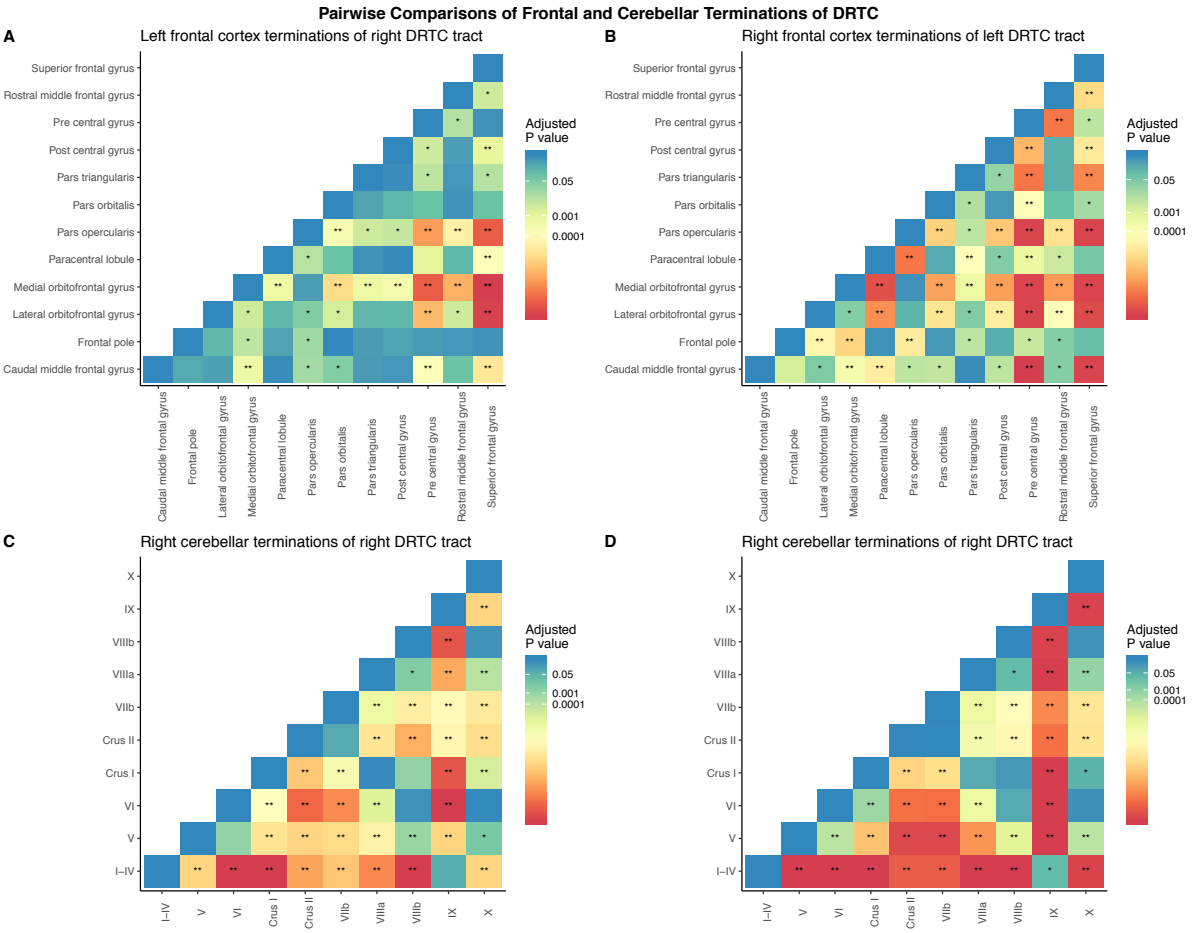


**Figure 5**. Heatmaps of pairwise comparisons for frontal (**A**, **B**) and cerebellar (**C**, **D**) terminations of DRTC tract. Pairwise comparisons performed with Wilcoxon signed rank test. *, statistical significance at $\alpha = 0.05$; **, statistical significance at $\alpha = 0.001$.

## Spatial topography of the proximal DRTC tract

Figure 6 shows all subjects' DRTC streamlines on a group template FA map, colour coded according to their region of frontal termination (colours used in Figure 6C/D are the same as those in Figure 4A/B). At the level of the SCP, by selecting frontal regions with the highest streamline density, it appears that streamlines terminating in the superior frontal gyrus are located more dorsally in the SCP (Figure 6A, middle slice), and more medially, best appreciated in sections along the long axis of the SCP (Figure 6B). This is confirmed by visualisation of the average streamline position for these two regions (Figure 6C/D).

Average streamline positions were calculated based on concatenated streamline bundles terminating in each frontal region for all subjects. For the left DRTC bundles, median (range) TSC was 3559 (884 – 73299). For the right DRTC bundles, median (range) TSC was 2516 (554 – 27643).

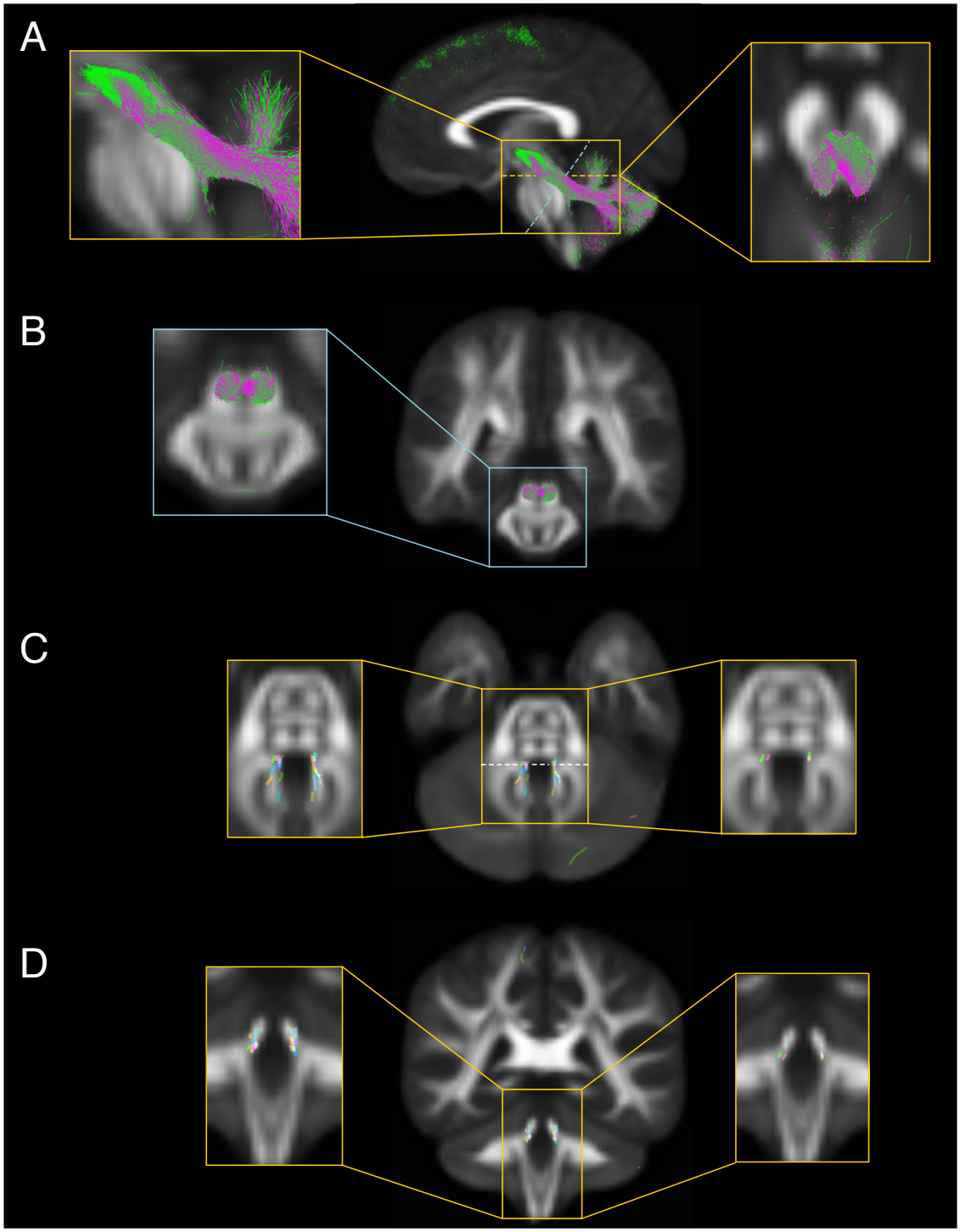


**Figure 6**. Spatial topography of the DRTC at the SCP shown on group template FA maps. **A**, **centre**: Parasagittal section through the left SCP, showing overlaid DRTC bundles of 30 subjects projecting to right precentral gyrus (green) and right superior frontal gyrus (pink). **A**, **left inlay**: enlarged parasaggital section. **A**, **right inlay**: enlarged axial section through mid-SCP, along yellow dotted line. **B**, Cross-section through the SCP at the level of the blue dotted line in A, showing overlaid bilateral DRTC bundles of 30 subjects projecting to right precentral gyrus (green) and superior frontal gyrus (pink). **B**, **left inlay**: enlarged view of same. **C**, **centre**: axial section at level of proximal SCP, centre. **C**, **left inset**: average streamline positions of DRTC bundles terminating in all regions of contralateral frontal cortices, with colour notation as per Figure 4A. **C**, **right inset**: average streamline positions of left DRTC bundles terminating in precentral gyrus (green) and superior frontal gyrus (pink). **D**, **centre**: coronal section at level of proximal SCP in plane of dotted white line in C, showing the average streamline position of DRTC bundles terminating in all regions of contralateral frontal cortex, with colour notation as per Figure 4A. **D**, **left inset**: enlarged view of same. **D**, **right inset**: average streamline positions of DRTC bundles terminating in precentral gyrus (green) and superior frontal gyrus (pink).

## Voxel-wise diffusion metrics

Figure 7 shows measures of voxel-wise diffusion microstructure metrics across the control cohort. FA was highest in the SCPs (left SCP mean ± S.D. 0.664 ± 0.0683; right SCP 0.638 ± 0.0597; t test p=0.378), lowest in the RN (left RN 0.288 ± 0.0710; right RN 0.305 ± 0.0777; p=0.548), with the average FA across the whole DRTC tract somewhere in between (left DRTC 0.441 ± 0.932; right DRTC 0.429 ± 0.0681; p=0.558). Values for mean diffusivity (MD) followed the same pattern, and again were higher in the SCP (left SCP 0.844 ± 0.070 $10^{-3}$ $mm^2/s$; right SCP 0.867 ± 0.072 $10^{-3}$ $mm^2/s$; p=0.663), lower in the RN (left RN 0.589 ± 0.026 $10^{-3}$ $mm^2/s$; right RN 0.593 ± 0.029 $10^{-3}$ $mm^2/s$; p=0.759), and averaged across the whole DRTC were 0.644 ± 0.028 $10^{-3}$ $mm^2/s$ (left) and 0.642 ± 0.037 $10^{-3}$ $mm^2/s$ (right), with no group difference between sides (p=0.759). The mean $V_{int}$ was 0.563 ± 0.0799, with little variation by side, ROI or whole tract (Figure 7C; p>0.78 for all regions). ODE across the DRTC followed a very similar distribution to that of FA. ODE was highest in the SCP (left SCP 0.868 ± 0.125, right SCP 0.816 ± 0.107; p=0.261), lowest in the RN (left RN 0.238 ± 0.077, right RN 0.244 ± 0.078; p=0.759), and mean ± S.D. whole-DRTC ODE was 0.461 ± 0.124 on the left, and 0.428 ± 0.075 on the right, with no group difference between sides (p=0.320).

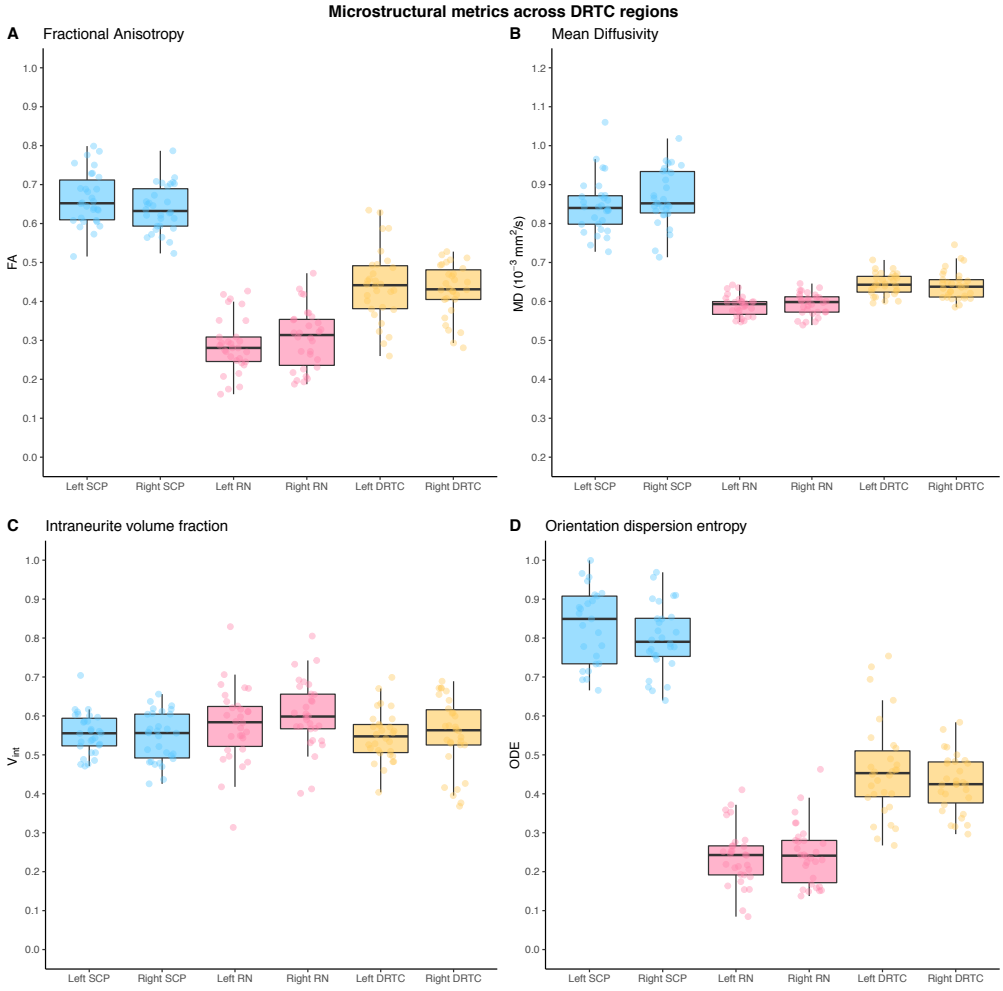

**Figure 7**. Box and dot plots showing DTI and SMT metrics across DRTC ROIs in thirty control subjects: the superior cerebellar peduncle (SCP), the red nucleus (RN) and averaged across the whole DRTC tract. **A**, fractional anisotropy; **B**, mean diffusivity; **C**, intraneurite volume fraction; **D**, orientation dispersion entropy.

## Reproducibility analysis

In order to assess the reproducibility of our findings, portions of the above analysis were applied to data from subjects who had been scanned twice, a week apart. After implementation of the aforementioned tractography pipeline to each subject's diffusion MRI data, quantitative streamline density analysis revealed good concordance within regions, from scan to rescan (Figure 8). There were no statistically significant differences in streamline density between the two timepoints at group level, even for those which appeared to diverge on visual inspection of boxplot data. ICC values varied across brain regions (Table 1). Mean ICC was highest for connections of the left DRTC from the left cerebellar cortex (mean ± S.D. 0.780 ± 0.188), and lowest for connections of the right DRTC from the right cerebellar cortex (0.475 ± 0.455). Using cutoffs as described by Koo & Li (Koo and Li 2016), the majority were rated as moderate or good (30/44, 68.2%). In 5 of these 30 brain regions, the calculated *p* value did not reach a level of statistical significance; in other words, there was a high probability that the observed ICC value occurred by chance. There were two negative ICC values, for streamline densities pertaining to the right DRTC (-0.139 for streamlines to the left precentral gyrus, and -0.4 for streamlines to the right cerebellar lobule IX).

Voxel-wise diffusion metrics varied very little between scan and rescan within different ROIs or across the whole DRTC tract (Figure 9). There were no significant differences between the two timepoints at group level on paired Wilcoxon testing after multiple comparison correction, in FA, MD, $V_{int}$ or ODE.

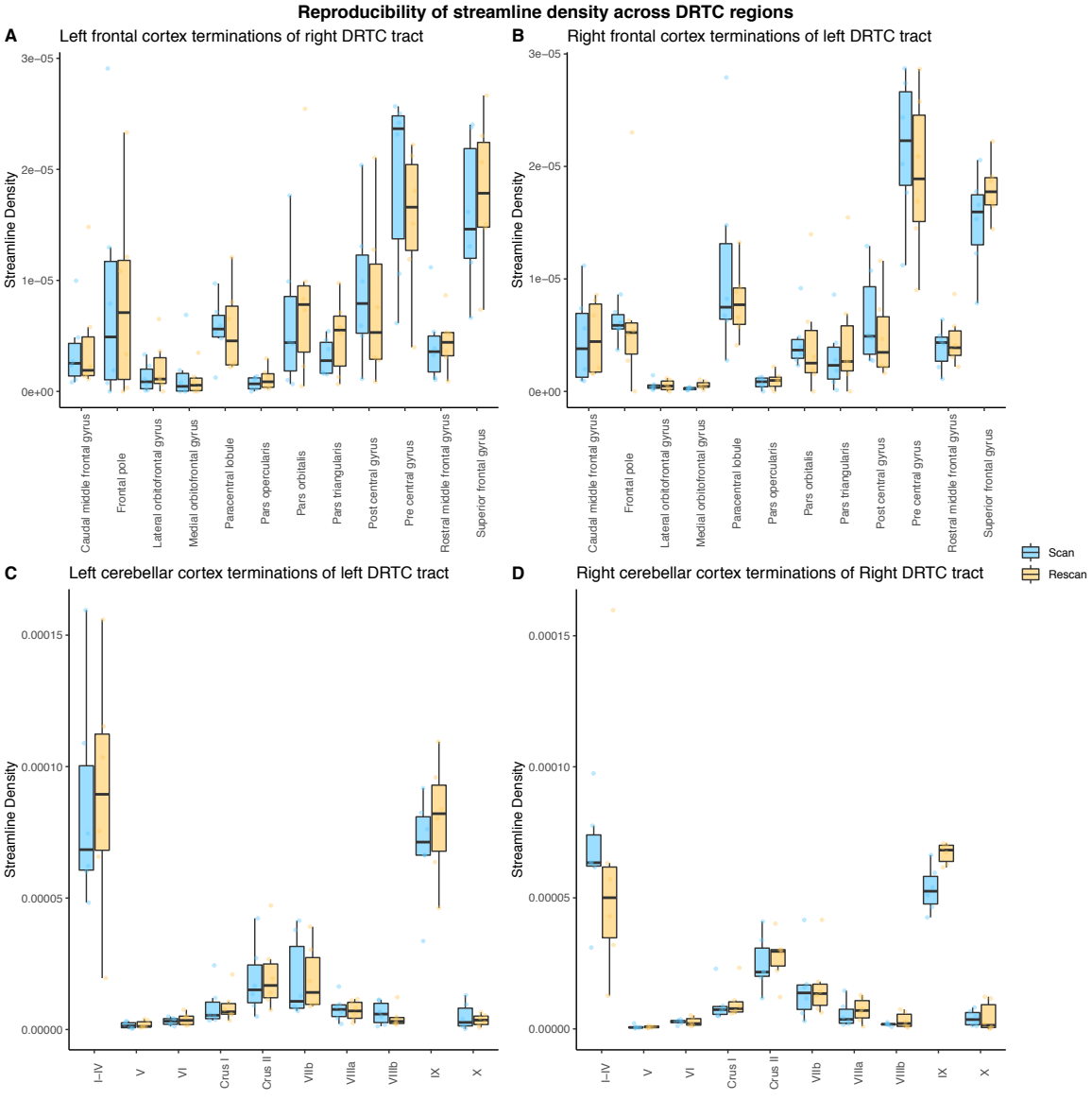


**Figure 8**. Box plots showing reproducibility of streamline density between scan and rescan. **A**, left frontal cortex terminations of right DRTC tract; **B**, right frontal cortex terminations of left DRTC tract; **C**, right cerebellar cortex terminations of right DRTC tract; **D**, left cerebellar cortex terminations of left DRTC tract.

| Region | R DRTC | | L DRTC | |
|---|---|---|---|---|
| | To L frontal cortex | | To R frontal cortex | |
| | ICC | p | ICC | p |
| Caudal middle frontal gyrus | ***0.89*** | ***0.002*** | ***0.917*** | ***0.001*** |
| Frontal pole | ***0.855*** | ***0.004*** | 0.166 | 0.344 |
| Lateral orbitofrontal gyrus | 0.619 | 0.054 | 0.386 | 0.175 |
| Medial orbitofrontal gyrus | ***0.760*** | ***0.015*** | -0.141 | 0.613 |
| Paracentral lobule | 0.212 | 0.306 | 0.495 | 0.109 |
| Pars opercularis | 0.219 | 0.300 | ***0.736*** | ***0.020*** |
| Pars orbitalis | ***0.825*** | ***0.006*** | ***0.795*** | ***0.010*** |
| Pars triangularis | 0.513 | 0.100 | ***0.761*** | ***0.015*** |
| Post central gyrus | ***0.613*** | ***0.049*** | ***0.798*** | ***0.010*** |
| Pre central gyrus | -0.139 | 0.612 | ***0.688*** | ***0.032*** |
| Rostral middle frontal gyrus | ***0.751*** | ***0.017*** | 0.506 | 0.103 |
| Superior frontal gyrus | ***0.767*** | ***0.014*** | 0.340 | 0.207 |
| *Mean ± S.D.* | 0.575 ± 0.319 | N/A | 0.537 ± 0.309 | N/A |
| | To R cerebellar cortex | | To L cerebellar cortex | |
| I – IV | 0.234 | 0.288 | ***0.876*** | ***0.002*** |
| V | ***0.672*** | ***0.036*** | 0.558 | 0.078 |
| VI | 0.158 | 0.351 | 0.792 | **0.010** |
| Crus I | ***0.973*** | ***<0.001*** | ***0.95*** | ***<0.001*** |
| Crus II | ***0.850*** | ***0.004*** | ***0.982*** | ***<0.001*** |
| VIIb | ***0.953*** | ***<0.001*** | ***0.958*** | ***<0.001*** |
| VIIIa | ***0.814*** | ***0.008*** | ***0.767*** | ***0.014*** |
| VIIIb | 0.07 | 0.428 | ***0.687*** | ***0.032*** |
| IX | -0.4 | 0.815 | ***0.829*** | ***0.006*** |
| X | 0.425 | 0.150 | 0.398 | 0.167 |
| *Mean ± S.D.* | 0.475 ± 0.455 | N/A | 0.780 ± 0.188 | N/A |

**Table 1**. Intraclass correlation coefficients for streamline density within regions for each subject between scan and rescan in reproducibility cohort. ICC values colour coded as good > 0.75 (n=21), moderate > 0.5 (n = 9), poor < 0.5 (n = 14). Entries in bold italics indicate significance at $\alpha = 0.05$. S.D., standard deviation.

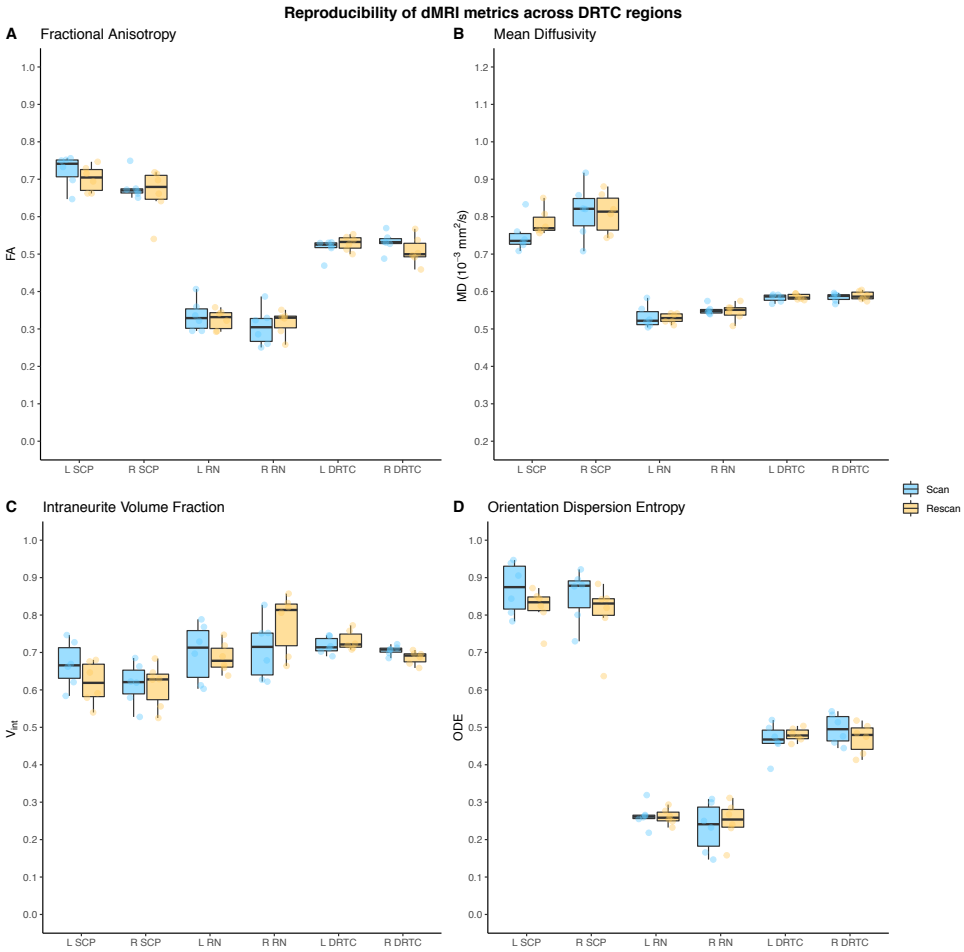


**Figure 9**. Box- and dot-plots showing good reproducibility of voxel-wise diffusion microstructure metrics between scan and rescan. **A**, fractional anisotropy; **B**, mean diffusivity; **C**, intraneurite volume fraction; D, orientation dispersion entropy across DRTC regions.

# Discussion

In this study we report a robust locally-seeded, subject-specific tractography pipeline to extract the DRTC tract in children, with a high degree of anatomical accuracy. DRTC connections to the precentral gyrus and superior frontal gyrus had the highest streamline density. In the cerebellum, the highest streamline density was for connections from lobules I-IV and lobule IX. There appears to be a spatial distribution of cerebellofrontal fibres within the SCP, which is the first time this has been shown. In particular, fibre groups terminating in the superior frontal gyrus were localised, on average, more dorsomedially within the SCP than those terminating in motor cortex. A separate analysis of scan-rescan data in older subjects indicates that the measures depicted in the control cohort (streamline density, DTI and SMT metrics) show a good inter-session reproducibility.

## Tractographic Anatomy of the DRTC

Several dMRI studies have depicted the anatomy of the DRTC tract in healthy adults using tractography. Early attempts utilised diffusion tensor-based tractography to show the projections of the SCP (which contains proximal DRTC fibres) (Salamon et al. 2007) as well as the entire extent of the DRTC (Kwon et al. 2011). The presence of a smaller, non-decussating, DRTC tract has also been demonstrated using microdissection-validated q-space imaging (Meola et al. 2016), though its function is yet to be described and it is not considered further here. A comprehensive consideration of CSD-based tractographic anatomy of cerebellofrontal projections was given by Palesi *et al.* (Palesi et al. 2015, 2016) who found that projections of this tract terminate predominantly in contralateral prefrontal cortex and associative areas, as judged on TSC. Honing in specifically on the frontal lobe, tensor-based probabilistic tractography showed that the dominant area in which DRTC fibres terminated (as judged on proportion of total DRTC streamlines) was Brodmann Area 6 (BA6) (Ji et al. 2019), a region containing the supplementary motor area (SMA). This finding confirmed earlier transneuronal viral transport studies elucidating projections from the dentate nuclei to the SMA in primates (Akkal et al. 2007). Our results provide some further supportive evidence for this work, although we demonstrate that the projection density of the DRTC to the superior frontal gyrus (containing the SMA) is in fact second to that of the precentral gyrus, as can be appreciated visually in Figure 3 and quantitatively in Figure 4A/B. This is also corroborated by the finding that DRTC streamlines passed through frontal- and motor-predominant thalamic areas (Figure 2B/C). The decision to use streamline density in this study could be considered methodologically superior to using TSC or streamline proportion as a metric, and may explain this discrepancy in cerebello-frontal connectivity. Without a consideration of the volume of cortical target regions, the method of Ji *et al.* (Ji et al. 2019) may have biased upwards the SMA fibre counts, as BA6 is a comparatively large region.

The present study is the first to describe the tractographic anatomy of the DRTC in its entirety in healthy children, spanning a wide age range from 7 to 21 years old. ‘Along-tract’ DTI metrics of the proximal DRTC in children have been reported previously (Leitner et al. 2015), showing that FA and MD vary across the long axis of the SCP. Furthermore, application of the same automated tractography tool to a larger cross-sectional cohort of children at different ages showed that mean tract-FA increased, while mean tract-MD decreased from infancy to adolescence (Bruckert et al. 2019), although there was no evidence that the gross anatomical structure of the cerebellar projections changed with age. Our results are the first to quantitatively describe the anatomy of DRTC projections to the frontal lobe in children, and we confirm that these are stable across the age spectrum studied here (Figure 2B/2C). These normative findings will be of use in supporting future quantitative dMRI analyses in patients of this age group.

The dominant areas from which cerebellar cortex streamlines contributed to the DRTC were the anterior cerebellum (Lobules I-IV), and Lobule IX. Pairwise comparison testing showed that these two

regions' streamline densities were significantly higher than all others, for right and left DRTC tracts (Figure 5C/D). This result is partially in agreement with that of Palesi *et al.* (Palesi et al. 2015), who, in their study on 15 healthy adults, showed that TSC to the anterior cerebellum was highest, but that TSC to the inferior lobule (IX-X) was much lower. This may point to divergent cerebellar connectivity of the tract between children and adults, although confirmation of this finding in a larger dataset using the same methodology would be required.

It is well-known that tractography is unable to provide information on the direction of observed connections or to identify synaptic nodes. *A priori* anatomical knowledge holds that projections from the Purkinje cells of the hemispheric cerebellar cortex synapse with neurons in the dentate nuclei (Haines and Dietrichs 2012), which can be viewed as a crucial node in the cerebello-cerebral network. Indeed, the streamlines coursing from cerebellar cortex to frontal cortex shown in this study are falsely continuous as they include not only the DRTC but also this important corticonuclear projection. Sub-millimetric dMRI at 7T has been used to map these cerebellar corticonuclear projections (Steele et al. 2017), showing that the dentate nucleus contains topographic connectivity from motor and non-motor cerebellar regions. Studies of anterograde dentate projections have provided evidence of a topographic organisation at the level of the cerebral cortex from viral tracer studies in primates (Dum and Strick 2003). More recently, resting-state functional MRI has shown that human dentate nuclei obey principles of functional organisation seen in other major subcortical structures, with three distinct territories contributing to primary, attentional and default-mode processing (Guell et al. 2020).

Few studies to date have investigated the precise arrangement of fibres within cerebellar white matter. A post-mortem HARDI tractography study revealed differential pontocerebellar projections in the middle cerebellar peduncle (Takahashi et al. 2013), a white matter structure much larger than the SCP, which conveys afferent information to the cerebellum. A small clinicopathological lesion study in humans showed a somatotopic correspondence in the SCP with fibres from the dentate nucleus (Ben Hamida and Lapresle 1969). However, the present study is the first to show a 'fronto-topic' organisation of anterograde connections to distinct frontal cortex regions, at the level of the SCP. Figures 6C/D show the average streamline positions of each DRTC bundle. These streamline positions were averaged across thousands of summed subject-specific streamlines (median TSC, 2516 and 3559 for right and left DRTC bundles, respectively), strengthening the robustness of the insight. To the best of the authors' knowledge, there have been no recorded histological validations of this pattern of arrangement in the SCP.

Knowledge of this fronto-topic pattern of arrangement could have considerable implications in surgery of the fourth ventricle, where the SCP is visualised and manipulated during tumour resection. Around a quarter of children undergoing such surgery develop CMS (Toescu et al. 2020), which may be partially explained by the fact that some of the most medial fibres – and therefore most likely to be manipulated – in the SCP are those projecting to the superior frontal gyrus, containing the SMA.

Clinical parallels have been drawn between the SMA syndrome, seen more commonly in adults following parasaggital tumour resection, and CMS (Grønbæk et al. 2020), as both present with transient mutism. This hypothesis requires testing in a clinical cohort, and application of sophisticated tractography post-processing such as shape analysis (Glozman et al. 2018; Yeh 2020) could yield further clinically relevant insights.

## Microstructural metrics of DRTC tract

The diffusion tensor and spherical mean technique were used to interrogate the microstructural properties along the DRTC tract. FA and ODE were highest in the SCP, lowest in the RN, with the average metric across the whole DRTC lying between the two. This finding is to be expected given the histological makeup of the SCP (white matter) and the RN (grey matter). FA, however, encodes both the microscopic diffusion process as well as the distribution of neurite orientations. SMT is able to separate out these two confounding effects and quantitatively estimate the ODE, a measure of the dispersion of neurite orientations. The similarity of the results for FA and ODE indicates that FA in the regions assessed is to a large extent determined by orientational tissue structure (such as fibre crossings and orientation dispersion), rather than neurite density . Beyond this, the ODE assumed more extreme values than FA in the two ROIs, possibly indicating a greater contrast in distinguishing orientational tissue properties. This metric may therefore show promise as a biomarker in acquired pathologies affecting the DRTC. The brains of healthy children do not show any statistically significant differences in microstructural metrics between sides for each region of the DRTC, indicating that lateralised discrepancies of FA described in the SCP in CMS (Law et al. 2012; Van Baarsen et al. 2013) may be highly relevant.

The low ODE in the RN indicates a high degree of fibre dispersion consistent with this region as a synaptic point in the DRTC tract, and the complex arborisation patterns seen in cerebellorubral neurons (Shinoda et al. 1988). The RN is also a region of high iron content. The non-haem intracellular iron is mostly sequestered as ferritin (Hallgren and Sourander 1958), with a smaller labile pool of metabolically active ferric ($Fe^{3+}$) contributing to neurotransmission. The T2 shortening this iron load causes likely explains the finding of higher than expected $V_{int}$ in the RN.

## Reproducibility analyses

dMRI acquisitions are subject to random noise which itself is variable across sessions. Even with the same subjects, scanner and downstream analysis pipeline, some variability is to be expected in the data. Therefore it is important to assess the scan-rescan reliability of the analysis in order to strengthen the conclusions to be drawn. The terminology surrounding reproducibility and replicability is nuanced, and in this report the authors are concerned mainly with “methods reproducibility”, namely providing “sufficient detail about procedures and data so that the same procedures could be exactly repeated” (Plesser 2018).

Figures 8 and 9 demonstrate little variability in the chosen metrics (streamline density, FA, MD, $V_{int}$ and ODE) at group level, with no significant differences observed from scan to rescan. The majority of ICC values for scan-rescan streamline density were greater than 0.5, indicating a good level of consistency of this metric across scanning sessions. Twenty-five of 30 good/moderate ICC ratings returned a *p* value of <0.05, indicating a low probability of having observed these values by chance, were the null hypothesis true. The two negative ICC values in the results were found in two regions thought to have the highest streamline density (left precentral gyrus and left cerebellar lobule IX), and the authors recognise that this tempers these results somewhat. In these two cases the null hypothesis (ICC = 0) cannot be rejected, which suggests that the negative values were observed by chance.

Even with *post-hoc* controls such as reproducibility analyses, there is no guarantee of correct results, due to the inherent limitations of the tractography algorithm on which the results are based (Nath et al. 2020; Yeh 2020). What is afforded by demonstrating good scan-rescan reliability is a high degree of *internal* validity of the results. External validity of the results can only be shown by applying the methodology to a separate cohort of patients, ideally with brain pathology, and with the use of a different tractography algorithm.

## Methodological considerations

Several methodological points in this study bear further examination. The anatomically accurate reconstruction of decussating, multi-synaptic pathways such as the DRTC tracts is complex and choices are to be made at each step of the pipeline. Firstly, in acquisition, a multi-shell protocol with *b*-values up to 2200 s/mm$^2$ was employed which provided higher angular resolution to resolve crossing fibre distributions by enabling the application of CSD modelling to recover underlying FODs. CSD is better able to resolve crossing fibres within a voxel (a scenario encountered in the mesencephalic decussation of the DRTCs) than the diffusion tensor, is able to tolerate less exhaustive sampling than diffusion spectrum imaging, and is computationally efficient. Furthermore, scans were acquired on a clinically-equipped scanner with a short total acquisition time, making clinical translation highly feasible.

Secondly, with regards to regions of interest, the dentate nucleus itself was not chosen as the seed point as its boundaries proved difficult to demarcate with low-resolution dMRI data. The SCP was chosen as the seed point as almost all fibres emanating from the dentate pass through it; it can be clearly delineated as it is bounded by CSF medially (fourth ventricle) and laterally (parabrachial recess); and its identification is aided by high-contrast ‘super-resolution’ track-density imaging reconstructions (Figure 2A). This decision, as well as the waypoint ROI placement at the RN, was influenced by the detailed methodological descriptions of Palesi *et al.* (Palesi et al. 2016). In contrast

to other methods of reconstructing DRTC tracts, using thalamic waypoints (Van Baarsen et al. 2013) or cortical seed points (Akram et al. 2018), SCP seed and RN waypoint ROIs leave the most rostral and caudal ends of the tract relatively unconstrained and thus avoid imposing anatomical priors on these regions of the tract where its variability is highest.

Streamlines derived from tractography are mathematical approximations of the underlying orientation information inherent in dMRI data. The scale probed by diffusion imaging is several orders of magnitude higher than that of biophysical neural elements, therefore to view streamlines as analogous to underlying neuronal projections is fallacious. Carefully executed tractography is the only technique with which to infer long-range structural associations between brain regions *in vivo*. Yet difficulties are introduced when attempts are made to quantify the strength of connection between two different brain regions (Smith et al. 2020), and, as stated emphatically by Jones (Jones et al. 2013), tractography is not able to provide a directly quantitative estimate of connection strength. Recent developments in tractogram filtering algorithms (Pestilli et al. 2014; Smith et al. 2015; Girard et al. 2017) will optimise our ability to quantify connection strengths across multiple brain regions and subjects, although these were designed primarily for use in whole-brain tractography in the setting of connectomics studies. The authors recognise the methodological limitation of this work due to having not applied such tractogram post-processing. However the method described here is a modest improvement on a previous attempt to quantify cerebello-frontal connectivity via the DRTC which simply used proportions of raw streamline count (Ji et al. 2019). The estimates of connectivity provided herein are based on a heavily supervised, locally-seeded tractography pipeline that accurately recapitulates the known underlying anatomy in an internally reproducible fashion. Furthermore, our description is the first to assess these metrics in a paediatric cohort.

## Conclusions

A robust locally-seeded tractography pipeline is described to extract the DRTC tracts in healthy children. Quantitative tractographic data is leveraged to provide the first evidence towards a fronto-topic organisation of anterograde projections to the frontal cortex at the level of the SCP. DTI parameters and the novel metrics of $V_{int}$ and ODE, derived from the spherical mean technique, are described in regions of and across the DRTC for the first time. A separate reproducibility analysis showed good consistency and no group differences in the dMRI metrics described. These novel anatomical insights into this well-studied pathway may prove to be of clinical relevance in the surgical resection of cerebellar tumours.

# Funding

This work was supported by Great Ormond Street Hospital Children's Charity (grant number 174385 to S.M.T.) and by Children with Cancer UK (grant number CwC-UK-15-203 to P.W.H.).

# Acknowledgements

All research at Great Ormond Street Hospital NHS Foundation Trust and UCL Great Ormond Street Institute of Child Health is made possible by the NIHR Great Ormond Street Hospital Biomedical Research Centre.

# References

Akkal D, Dum RP, Strick PL. 2007. Supplementary motor area and presupplementary motor area: Targets of basal ganglia and cerebellar output. J Neurosci. 27:10659–10673.

Akram H, Dayal V, Mahlknecht P, Georgiev D, Hyam J, Foltynie T, Limousin P, De Vita E, Jahanshahi M, Ashburner J, Behrens T, Hariz M, Zrinzo L. 2018. Connectivity derived thalamic segmentation in deep brain stimulation for tremor. NeuroImage Clin. 18:130–142.

Andersson JLR, Skare S, Ashburner J. 2003. How to correct susceptibility distortions in spin-echo echo-planar images: application to diffusion tensor imaging. Neuroimage. 20:870–888.

Andersson JLR, Sotiropoulos SN. 2016. An integrated approach to correction for off-resonance effects and subject movement in diffusion MR imaging. Neuroimage. 125:1063–1078.

Auerbach EJ, Xu J, Yacoub E, Moeller S, Uğurbil K. 2013. Multiband accelerated spin-echo echo planar imaging with reduced peak RF power using time-shifted RF pulses. Magn Reson Med. 69:1261–1267.

Basser PJ, Mattiello J, LeBihan D. 1994. MR diffusion tensor spectroscopy and imaging. Biophys J. 66:259–267.

Behrens TEJ, Johansen-Berg H, Woolrich MW, Smith SM, Wheeler-Kingshott CAM, Boulby PA, Barker GJ, Sillery EL, Sheehan K, Ciccarelli O, Thompson AJ, Brady JM, Matthews PM. 2003. Non-invasive mapping of connections between human thalamus and cortex using diffusion imaging. Nat Neurosci. 6:750–757.

Ben Hamida M, Lapresle J. 1969. Correspondance somatotopique chez l'homme des degenerescences segmentaires du pedoncule cerebelleux superieur secondaires a des lesions limitees du noyau dentele homolateral. Rev Neurol. 120:263–267.

Benjamini Y, Hochberg Y. 1995. Controlling the False Discovery Rate: A Practical and Powerful Approach to Multiple Testing. J R Stat Soc Ser B.

Bruckert L, Shpanskaya K, McKenna ES, Borchers LR, Yablonski M, Blecher T, Ben-Shachar M, Travis KE, Feldman HM, Yeom KW. 2019. Age-Dependent White Matter Characteristics of the Cerebellar Peduncles from Infancy Through Adolescence. The Cerebellum. 1–16.

Calamante F, Tournier J-D, Jackson GD, Connelly A. 2010. Track-density imaging (TDI): super-resolution white matter imaging using whole-brain track-density mapping. Neuroimage. 53:1233–1243.

Calamante F, Tournier JD, Heidemann RM, Anwander A, Jackson GD, Connelly A. 2011. Track density imaging (TDI): Validation of super resolution property. Neuroimage. 56:1259–1266.

Clayden JD, King MD, Maniega SM, Bastin ME, Storkey AJ, Clark CA. 2011. TractoR: Magnetic resonance imaging and tractography with R. J Stat Softw. 44:1–18.

Dale AM, Fischl B, Sereno MI. 1999. Cortical Surface-Based Analysis. Neuroimage. 9:179–194.

Diedrichsen J. 2006. A spatially unbiased atlas template of the human cerebellum. Neuroimage. 33:127–138.

Dum RP, Strick PL. 2003. An unfolded map of the cerebellar dentate nucleus and its projections to the cerebral cortex. J Neurophysiol. 89:634–639.

Fischl B, Salat DH, Busa E, Albert M, Dieterich M, Haselgrove C, Van Der Kouwe A, Killiany R, Kennedy D, Klaveness S, Montillo A, Makris N, Rosen B, Dale AM. 2002. Whole brain segmentation: Automated labeling of neuroanatomical structures in the human brain. Neuron. 33:341–355.

Gamer M, Lemon J, Fellows I, Singh P. 2019. irr: Various Coefficients of Interrater Reliability and Agreement.

Girard G, Daducci A, Petit L, Thiran JP, Whittingstall K, Deriche R, Wassermann D, Descoteaux M. 2017. AxTract: Toward microstructure informed tractography. Hum Brain Mapp. 38:5485–5500.

Glozman T, Bruckert L, Pestilli F, Yecies DW, Guibas LJ, Yeom KW. 2018. Framework for shape analysis of white matter fiber

bundles. Neuroimage. 167:466–477.
Grønbæk J, Molinari E, Avula S, Wibroe M, Oettingen G, Juhler M. 2020. The supplementary motor area syndrome and the cerebellar mutism syndrome: a pathoanatomical relationship? Child's Nerv Syst. 36:1197–1204.
Guell X, D'Mello AM, Hubbard NA, Romeo RR, Gabrieli JDE, Whitfield-Gabrieli S, Schmahmann JD, Anteraper SA. 2020. Functional Territories of Human Dentate Nucleus. Cereb Cortex. 30:2401–2417.
Haines DE, Dietrichs E. 2012. The cerebellum - structure and connections. 1st ed, Handbook of Clinical Neurology. Elsevier B.V.
Hallgren B, Sourander P. 1958. THE EFFECT OF AGE ON THE NON-HAEMIN IRON IN THE HUMAN BRAIN. J Neurochem. 3:41–51.
Jenkinson M, Beckmann CF, Behrens TEJ, Woolrich MW, Smith SM. 2012. FSL. Neuroimage. 62:782–790.
Jeurissen B, Tournier J-D, Dhollander T, Connelly A, Sijbers J. 2014. Multi-tissue constrained spherical deconvolution for improved analysis of multi-shell diffusion MRI data. Neuroimage. 103:411–426.
Ji Q, Edwards A, Glass JO, Brinkman TM, Patay Z, Reddick WE. 2019. Measurement of Projections Between Dentate Nucleus and Contralateral Frontal Cortex in Human Brain Via Diffusion Tensor Tractography. The Cerebellum. 1–9.
Jones DK, Knösche TR, Turner R. 2013. White matter integrity, fiber count, and other fallacies: The do's and don'ts of diffusion MRI. Neuroimage.
Kaden E, Kelm ND, Carson RP, Does MD, Alexander DC. 2016. Multi-compartment microscopic diffusion imaging. Neuroimage. 139:346–359.
Kaden E, Kruggel F, Alexander DC. 2016. Quantitative mapping of the per-axon diffusion coefficients in brain white matter. Magn Reson Med. 75:1752–1763.
Kassambara A. 2019. ggpubr: 'ggplot2' Based Publication Ready Plots.
Kassambara A. 2020. rstatix: Pipe-Friendly Framework for Basic Statistical Tests.
Kellner E, Dhital B, Kiselev VG, Reisert M. 2016. Gibbs-ringing artifact removal based on local subvoxel-shifts. Magn Reson Med. 76:1574–1581.
Koo TK, Li MY. 2016. A Guideline of Selecting and Reporting Intraclass Correlation Coefficients for Reliability Research. J Chiropr Med. 15:155–163.
Kwon HG, Hong JH, Hong CP, Lee DH, Ahn SH, Jang SH. 2011. Dentatorubrothalamic tract in human brain: Diffusion tensor tractography study. Neuroradiology. 53:787–791.
Law N, Greenberg M, Bouffet E, Taylor MD, Laughlin S, Strother D, Fryer C, McConnell D, Hukin J, Kaise C, Wang F, Mabbott DJ. 2012. Clinical and neuroanatomical predictors of cerebellar mutism syndrome. Neuro Oncol. 14:1294–1303.
Leitner Y, Travis KE, Ben-Shachar M, Yeom KW, Feldman HM. 2015. Tract Profiles of the Cerebellar White Matter Pathways in Children and Adolescents. The Cerebellum. 14:613–623.
McEvoy SD, Lee A, Poliakov A, Friedman S, Shaw D, Browd SR, Ellenbogen RG, Ojemann JG, Mac Donald CL. 2016. Longitudinal cerebellar diffusion tensor imaging changes in posterior fossa syndrome. NeuroImage Clin. 12:582–590.
Meola A, Comert A, Yeh F, Sivakanthan S, Fernandez-Mi. 2016. The nondecussating pathway of the dentatorubrothalamic tract in humans: human connectome-based tractographic study and microdissection validation. J Neurosurg. 124:1406–1412.
Modat M, Cash DM, Daga P, Winston GP, Duncan JS, Ourselin S. 2014. Global image registration using a symmetric block-matching approach. J Med Imaging. 1:024003.
Mollink J, van Baarsen KM, Dederen PJWC, Foxley S, Miller KL, Jbabdi S, Slump CH, Grotenhuis JA, Kleinnijenhuis M, van Cappellen van Walsum AM. 2016. Dentatorubrothalamic tract localization with postmortem MR diffusion tractography compared to histological 3D reconstruction. Brain Struct Funct. 221:3487–3501.
Morris EB, Phillips NS, Laningham FH, Patay Z, Gajjar A, Wallace D, Boop F, Sanford R, Ness KK, Ogg RJ. 2009. Proximal dentatothalamocortical tract involvement in posterior fossa syndrome. Brain. 132:3087–3095.
Mugler JP, Brookeman JR. 1990. Three-dimensional magnetization-prepared rapid gradient-echo imaging (3D MP RAGE). Magn Reson Med. 15:152–157.
Nath V, Schilling KG, Parvathaneni P, Huo Y, Blaber JA, Hainline AE, Barakovic M, Romascano D, Rafael-Patino J, Frigo M, Girard G, Thiran J, Daducci A, Rowe M, Rodrigues P, Prčkovska V, Aydogan DB, Sun W, Shi Y, Parker WA, Ould Ismail

AA, Verma R, Cabeen RP, Toga AW, Newton AT, Wasserthal J, Neher P, Maier-Hein K, Savini G, Palesi F, Kaden E, Wu Y, He J, Feng Y, Paquette M, Rheault F, Sidhu J, Lebel C, Leemans A, Descoteaux M, Dyrby TB, Kang H, Landman BA. 2020. Tractography reproducibility challenge with empirical data (TraCED): The 2017 ISMRM diffusion study group challenge. J Magn Reson Imaging. 51:234–249.

Palesi F, De Rinaldis A, Castellazzi G, Calamante F, Muhlert N, Chard D, Tournier JD, Magenes G, D'Angelo E, Wheeler-Kingshott CAMG. 2017. Contralateral cortico-ponto-cerebellar pathways reconstruction in humans in vivo: Implications for reciprocal cerebro-cerebellar structural connectivity in motor and non-motor areas. Sci Rep. 7:1–13.

Palesi F, Tournier J-D, Calamante F, Muhlert N, Castellazzi G, Chard D, D'Angelo E, Wheeler-Kingshott CG. 2016. Reconstructing contralateral fiber tracts: methodological aspects of cerebello-thalamocortical pathway reconstruction. Funct Neurol. 31:229–238.

Palesi F, Tournier JD, Calamante F, Muhlert N, Castellazzi G, Chard D, D'Angelo E, Wheeler-Kingshott CAM. 2015. Contralateral cerebello-thalamo-cortical pathways with prominent involvement of associative areas in humans in vivo. Brain Struct Funct. 220:3369–3384.

Perreault S, Lober RM, Cheshier S, Partap S, Edwards MS, Yeom KW. 2014. Time-dependent structural changes of the dentatothalamic pathway in children treated for posterior fossa tumor. Am J Neuroradiol. 35:803–807.

Pestilli F, Yeatman JD, Rokem A, Kay KN, Wandell BA. 2014. Evaluation and statistical inference for human connectomes. Nat Methods. 11:1058–1063.

Plesser HE. 2018. Reproducibility vs. Replicability: A Brief History of a Confused Terminology. Front Neuroinform. 11:76.

Salamon N, Sicotte N, Drain A, Frew A, Alger JR, Jen J, Perlman S, Salamon G. 2007. White matter fiber tractography and color mapping of the normal human cerebellum with diffusion tensor imaging. J Neuroradiol. 34:115–128.

Schilling KG, Daducci A, Maier-Hein K, Poupon C, Houde JC, Nath V, Anderson AW, Landman BA, Descoteaux M. 2019. Challenges in diffusion MRI tractography – Lessons learned from international benchmark competitions. Magn Reson Imaging. 57:194–209.

Schmahmann JD, Doyon J, Toga AW, Petrides M, Evans A. 2000. MRI atlas of the human cerebellum. San Diego (CA): Academic Press.

Shinoda Y, Futami T, Mitoma H, Yokota J. 1988. Morphology of single neurones in the cerebello-rubrospinal system. Behav Brain Res. 28:59–64.

Smith RE, Raffelt D, Tournier J, Connelly A. 2020. Quantitative streamlines tractography : methods and inter-subject normalisation. bioRxiv. 1–27.

Smith RE, Tournier J-D, Calamante F, Connelly A. 2015. SIFT2: Enabling dense quantitative assessment of brain white matter connectivity using streamlines tractography. Neuroimage. 119:338–351.

Smith RE, Tournier JD, Calamante F, Connelly A. 2012. Anatomically-constrained tractography: Improved diffusion MRI streamlines tractography through effective use of anatomical information. Neuroimage. 62:1924–1938.

Smith SM, Jenkinson M, Woolrich MW, Beckmann CF, Behrens TEJ, Johansen-Berg H, Bannister PR, De Luca M, Drobnjak I, Flitney DE, Niazy RK, Saunders J, Vickers J, Zhang Y, De Stefano N, Brady JM, Matthews PM. 2004. Advances in functional and structural MR image analysis and implementation as FSL. Neuroimage. 23:S208–S219.

Soelva V, Hernáiz Driever P, Abbushi A, Rueckriegel S, Bruhn H, Eisner W, Thomale U-W. 2013. Fronto-cerebellar fiber tractography in pediatric patients following posterior fossa tumor surgery. Childs Nerv Syst. 29:597–607.

Steele CJ, Anwander A, Bazin PL, Trampel R, Schaefer A, Turner R, Ramnani N, Villringer A. 2017. Human cerebellar sub-millimeter diffusion imaging reveals the motor and non-motor topography of the dentate nucleus. Cereb Cortex. 27:4537–4548.

Takahashi E, Song JW, Folkerth RD, Grant PE, Schmahmann JD. 2013. Detection of postmortem human cerebellar cortex and white matter pathways using high angular resolution diffusion tractography: A feasibility study. Neuroimage. 68:105–111.

Team RC. 2017. R: A language and environment for statistical computing.

Toescu S, Samarth G, Layard Horsfall H, Issitt R, Margetts B, Phipps K, Jeelani N, Thompson D, Aquilina K. 2020. Fourth ventricle tumours in children – complications and influence of surgical approach. J Neurosurg Pediatr.

Tournier J-D, Calamante F, Connelly A. 2010. Improved probabilistic streamlines tractography by 2nd order integration over fibre orientation distributions. Proc Int Soc Magn Reson Med. 1670.

Tournier J-D, Calamante F, Connelly A. 2012. MRtrix: Diffusion tractography in crossing fiber regions. Int J Imaging Syst Technol. 22:53–66.

Tournier J-D, Calamante F, Gadian DG, Connelly A. 2004. Direct estimation of the fiber orientation density function from diffusion-weighted MRI data using spherical deconvolution. Neuroimage. 23:1176–1185.

Van Baarsen K, Kleinnijenhuis M, Konert T, Van Cappellen Van Walsum AM, Grotenhuis A. 2013. Tractography demonstrates dentate-rubro-thalamic tract disruption in an adult with cerebellar mutism. Cerebellum. 12:617–622.

Veraart J, Novikov DS, Christiaens D, Ades-aron B, Sijbers J, Fieremans E. 2016. Denoising of diffusion MRI using random matrix theory. Neuroimage. 142:394–406.

Wickham H. 2009. ggplot2: Elegant Graphics for Data Analysis.

Yeh F-C. 2020. Shape Analysis of the Human Association Pathways. Neuroimage. 117329.

Zhang Y, Brady M, Smith S. 2001. Segmentation of brain MR images through a hidden Markov random field model and the expectation-maximization algorithm. IEEE Trans Med Imaging. 20:45–57.